Idealized four-wave mixing dynamics in a nonlinear Schrödinger equation fiber system

Anastasiia Sheveleva, Ugo Andral, Bertrand Kibler, Pierre Colman, J.M. Dudley, Christophe Finot

OPTICA

Idealized four-wave mixing dynamics in a nonlinear Schrödinger equation fiber system

Anastasiia Sheveleva,[1] Ugo Andral,[1] Bertrand Kibler,[1] Pierre Colman,[1] John M. Dudley,[2] and Christophe Finot[1,*]

[1]Laboratoire Interdisciplinaire Carnot de Bourgogne, UMR 6303 CNRS-Université de Bourgogne-Franche-Comté, 9 avenue Alain Savary, BP 47870, 21078, Dijon Cedex, France
[2]Institut FEMTO-ST, Université Bourgogne Franche-Comté CNRS UMR 6174, Besançon, 25000, France
*Corresponding author: christophe.finot@u-bourgogne.fr

Received 15 October 2021; revised 8 April 2022; accepted 11 April 2022; published 16 June 2022

The observation of ideal four-wave mixing dynamics is notoriously difficult to implement experimentally due to the generation of higher-order sidebands and optical loss, which limit the potential interaction distance. Here, we overcome this problem with an experimental technique that uses programmable phase and amplitude shaping to iterate the wave mixing initial conditions injected into an optical fiber. This extends the effective propagation distance by two orders of magnitude, allowing idealized Kerr-driven dynamics to be seen over 50 km of fiber using only one short fiber segment of 500 m. Our experiments reveal the full phase space topology, showing characteristic features of multiple Fermi–Pasta–Ulam recurrence, stationary wave existence, and the system separatrix representing the boundary between two distinct regimes of spatiotemporal evolution. Experiments are in excellent quantitative agreement with numerical solutions of the differential equation system describing the wave evolution. This experimental approach can be readily adapted to study other wave mixing and nonlinear propagation phenomena in optics.

https://doi.org/10.1364/OPTICA.445172

1. INTRODUCTION

The nonlinear Schrödinger equation (NLSE) is one of the seminal equations of science, describing wave evolution in a dispersive medium subject to an intensity-dependent nonlinear phase shift. It applies to many different domains including plasma physics, hydrodynamics, Bose–Einstein condensates, analog gravity, self-focusing and filamentation, and propagation in optical fiber [1].

The study of the nonlinear dynamics of the NLSE is a subject of very broad interest, and recent studies have yielded major advances in our understanding of processes such as symmetry breaking and Fermi–Pasta–Ulam (FPU) recurrence, as well as new insights into modulation instability [2–7]. The key physical process in the NLSE is nonlinear four-wave mixing (FWM), which arises from the dispersion-mediated energy exchange between discrete evolving frequency components [8]. From a fundamental perspective, the essential features of FWM are most clearly seen in the degenerate case when a single frequency pump generates only two sidebands of upshifted and downshifted frequency. In this case, the system is fully described by a reduced system of three coupled differential equations that fully capture the rich dynamical landscape [9]. This includes effects such as the initial phase of modulation instability, FPU recurrence, stationary waves (fixed points), and the separatrix (representing the boundary between different regimes of spatiotemporal evolution). However, although this canonical FWM system has been the subject of a number of previous theoretical and numerical studies, it is notoriously difficult to implement in practice.

Here, we address this shortcoming directly through a new experimental technique that allows us to characterize near-ideal FWM dynamics in a NLSE system based on optical fiber propagation. In particular, we have developed a system where iterated initial conditions are sequentially injected into an optical fiber, extending the effective propagation distance by two orders of magnitude and mitigating against unwanted sideband generation and optical loss. As a result, we are able to clearly follow the dynamical interactions among only four evolving frequency components over a distance of 50 km using only one fiber segment of only 500 m length. Our experiments reveal the full dynamical phase space topology, revealing characteristic features of multiple FPU recurrence cycles, stationary wave existence, and the system separatrix. We compare our experimental results with solutions of the canonical differential equation system describing the wave evolution, obtaining excellent agreement. This approach represents a significant improvement in both implementation and accuracy on previous approaches, and moreover, it can be readily generalized to the study of any arbitrary number of interacting wave components. This represents a major advance in the development of experimental techniques in nonlinear fiber optics.

2. THEORETICAL BACKGROUND AND PRINCIPLE

We first review the theoretical description of ideal FWM dynamics in the NLSE, and use numerical simulations to illustrate the expected dynamical behavior. In an ideal single mode and loss-free fiber, the evolution of a slowly varying electric field envelope $\psi(z, t)$ is governed by the NLSE

$$i\,\frac{\partial\psi}{\partial z} - \frac{\beta_2}{2}\frac{\partial^2\psi}{\partial t^2} + \gamma\,|\psi|^2\psi = 0, \tag{1}$$

with z being the propagation distance and t the time in a reference frame traveling at group velocity. The group velocity dispersion is β_2, and the nonlinear Kerr coefficient is γ. We can write the NLSE in normalized form:

$$i\,\frac{\partial A}{\partial \xi} + \frac{1}{2}\frac{\partial^2 A}{\partial \tau^2} + |A|^2 A = 0. \tag{2}$$

Here, normalized propagation and co-moving time variables ξ and τ are linked to the dimensional quantities in fiber optics by $\xi = z/L_{NL}$ and $\tau = t/\sqrt{|\beta_2|L_{NL}}$. The characteristic length scale is defined as $L_{NL} = (\gamma P_0)^{-1}$, with P_0 a power variable that in our case corresponds to the total average power of the evolving field, i.e., taking into account pump and any sideband components [9]. The normalized field is related to its dimensional equivalent $\psi(z, t)$ by $A(\xi, \tau) = \psi(z, t)/\sqrt{P_0}$. Note that this form of the NLSE that describes "focusing" dynamics is associated with a fiber dispersion parameter $\beta_2 < 0$.

We discuss the fundamental wave mixing processes in the NLSE by considering the injection of a modulated pump wave A_0 with two sidebands at frequencies $\pm\Omega$:

$$A(\xi, \tau) = A_0(\xi) + A_{-1}(\xi)\exp(i\Omega\tau) + A_1(\xi)\exp(-i\Omega\tau)\,. \tag{3}$$

Note that we omit the carrier frequency here, and the normalized frequency Ω is related to dimensional frequency f_m in Hz by $\Omega = 2\pi f_m\sqrt{|\beta_2|/\gamma P_0}$. In general, the injection of such a modulated signal in an optical fiber leads to the generation of multiple additional sidebands, but the ideal truncated FWM system that describes only pump and first sideband energy exchange with distance is described by only three coupled equations that are well known in the field of parametric amplification [10]:

$$\begin{cases} -i\frac{dA_0}{d\xi} = \left(|A_0|^2 + 2|A_{-1}|^2 + 2|A_1|^2\right)A_0 + 2A_{-1}A_1A_0^*, \\ -i\frac{dA_{-1}}{d\xi} + \frac{1}{2}\Omega^2 A_{-1} = \left(|A_{-1}|^2 + 2|A_0|^2 + 2|A_1|^2\right)A_{-1} + A_1^*A_0^2, \\ -i\frac{dA_1}{d\xi} + \frac{1}{2}\Omega^2 A_1 = \left(|A_1|^2 + 2|A_0|^2 + 2|A_{-1}|^2\right)A_1 + A_{-1}^*A_0^2. \end{cases} \tag{4}$$

When $|A_{\pm1}| \ll |A_0|$, amplification of the lateral sidebands can occur for $\Omega < 2$, with maximum gain at a frequency $\Omega = \Omega_0 = \sqrt{2}$. This is of course the same condition for maximum gain that is derived in the linear stability analysis of modulation instability [9]. Note also that even though this system describes degenerate FWM, the fact that there are only three frequency components involved has led to it being described (somewhat confusingly) as a "three wave" system.

Although solutions for the power [11] and phase [12] evolution of each component can be written in terms of elliptic functions, a significantly more intuitive picture of the dynamics is obtained using a Hamiltonian approach. Specifically, we associate the system with the one-dimensional conservative Hamiltonian

$$H = 2\eta(1-\eta)\,\cos\,\phi + \left(\Omega^2 + 1\right)\eta - \frac{3}{2}\eta^2, \tag{5}$$

with canonical conjugate variables $\eta = \eta(\xi)$ and $\phi = \phi(\xi)$ satisfying

$$\frac{\partial\eta}{\partial\xi} = \frac{\partial H}{\partial\phi} \quad \text{and} \quad \frac{\partial\phi}{\partial\xi} = -\frac{\partial H}{\partial\eta}, \tag{6}$$

and where η and ϕ are related to the amplitudes $A_k(\xi)$ and phases $\varphi_k(\xi)$ of the evolving sidebands ($k = 0,\ \pm1$) by

$$\begin{cases} \eta = \frac{|A_0|^2}{|A_0|^2+|A_{-1}|^2+|A_1|^2}, \\ \phi = \varphi_1 + \varphi_{-1} - 2\varphi_0. \end{cases} \tag{7}$$

Here, η and ϕ have physical interpretations as the fraction of total power in the central frequency component and the sideband–pump frequency component phase difference, respectively. Tracing the dynamics in the ($\eta\cos\phi$, $\eta\sin\phi$) plane fully captures all the physics of this ideal system.

To illustrate the physics of this system [13], Fig. 1 shows modeling results for different initial conditions. The parameters chosen correspond to maximum gain with $\Omega = \Omega_0$, and we assume initially equal sideband intensities $A_1(0)=A_{-1}(0)$. In Figs. 1(a) and (b), we show results of numerical integration of the ideal FWM system in Eq. (4) (blue), results from simulation of the segmented approach (described below) that we use in our experiments (red), and results from the numerical solution of the full multiwave interactions from the NLSE (yellow). In (c), we show the temporal evolution computed from Eq. (3) for the ideal FWM case.

We now discuss these results in detail. We first consider initial value $\eta_0 = 0.9$ and in-phase initial components ($\phi_0 = 0$ shown in Figs. 1(a1)–(c1)). The evolution of η in (1a) shows reversible energy transfer from the central mode to the sidebands, associated with expected FPU recurrence [2,14]. This recurrence is also seen in the temporal intensity profile in (c1), and is reflected in the closed trajectories in the phase space portrait in (b1). These orbits are on the right-hand side of the separatrix [dashed black line, also computed from Eq. (4)]. The separatrix divides the phase space into two regimes, and we see a qualitatively different evolution with different initial conditions of $\eta_0 = 0.9$ and $\phi_0 = \pi$. Although the power redistribution between modes remains periodic (a2), the amplitude variation is increased compared to the previous case. Moreover, the closed phase space trajectory (b2) is on the opposite side of the separatrix, associated with modified evolution as shown in (c2), with a temporal phase shift taking place in each recurrence cycle [2,15]. Indeed, comparing (c1) and (c2) illustrates the physical difference between trajectories on either side of the separatrix, and highlights the importance of the initial phase in driving the dynamics.

As a final example, Figs. 1(a3)–(c3) show the dynamics observed for $\eta_0 = 0.715$ and with $\phi_0 = 0$. This leads to a near-stationary solution with very low amplitude variation in the sideband ratio η (a3) and in the temporal intensity profile (c3). The phase space trajectory in this case is a closed orbit of very small effective radius, close to a fixed point of the system (b3).

Figures 1(a1)–(a3) also show the evolution of η computed from the numerical simulation of the full NLSE including multiple sideband generation (yellow). These results are clearly very different from the truncated ideal FWM system, with significantly more depletion of the central frequency component as additional sidebands are generated [4]. These differences are also very apparent when comparing the ideal FWM (blue) and NLSE (yellow) orbits in the phase space portraits in (b1)–(b3). In fact, we see that the

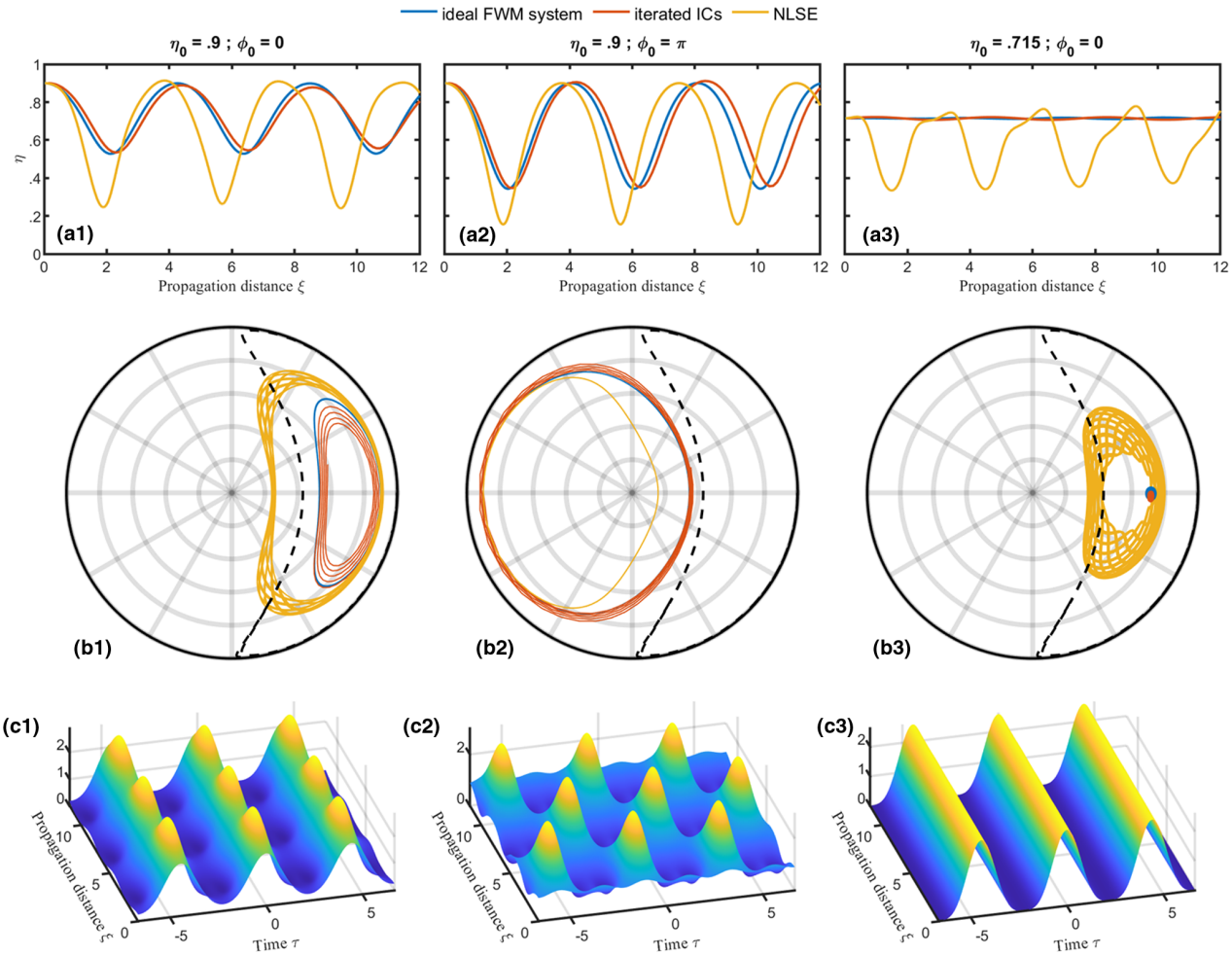

Fig. 1. Evolution properties of a strong pump and two lateral sidebands spaced by $\Omega = \Omega_0 = \sqrt{2}$. Results are shown for different initial conditions: (a1)–(c1) $\eta_0 = 0.9$ and $\phi_0 = 0$; (a2)–(c2) $\eta_0 = 0.9$, $\phi_0 = \pi$; (a3)–(c3) $\eta_0 = 0.715$ and $\phi_0 = 0$. Subpanels (a) show evolution of η for the ideal FWM system (blue), a segmented approach (red), and full NLSE (yellow). Subpanels (b) show the corresponding phase space portraits. Subpanels (c) show the corresponding evolution of the spatiotemporal intensity for the ideal FWM system $|A(\xi, \tau)|^2$, where $A(\xi, \tau)$ is given by Eq. (3) and consists of the total pump–sideband field.

NLSE orbits actually cross the separatrix associated with the ideal FWM system (this is in fact expected here given that the NLSE separatrix for this case is associated with the Akhmediev breather, which possesses an infinite number of sidebands). Moreover, for $\eta_0 = 0.715$, the stationary solution is clearly not recovered, and the orbit is much more complex than a fixed point.

These examples clearly show the difficulties in observing the canonical dynamics of ideal FWM in a NLSE system because of the generation of higher-order sidebands. Certainly, it is the cascading of the FWM process [16,17] that leads to important applications such as frequency-comb and supercontinuum generation, but their presence naturally means that the ideal FWM process cannot be studied in isolation. However, a segmented approach to propagation with reinjection of power-adjusted initial conditions allows us to overcome this limitation, and to develop a practical system that yields close to ideal FWM dynamics. The principle here is to replace a single long segment of fiber by a concatenation of segments that are sufficiently short such that additional sidebands cannot reach a significant level. Moreover, between sequential segments, we cancel spectral components outside the four principle modes, and we use amplification to restore the same average power. Results illustrating this segmented approach are shown as the red lines in Fig. 1, and clearly show how this approach yields excellent agreement with the ideal FWM model: all the main features previously discussed are now quantitatively reproduced. Note that for these results, we use fiber segment lengths of $\xi_L = 0.12$, a choice motivated by our experiments described in Section 4.

3. EXPERIMENTAL SETUP

Attempts to measure the complex longitudinal NLSE wave mixing dynamics in optical fiber have been previously reported using various methods such as destructive cut-back measurements [4], distributed optical time domain reflectometry [7,18,19], or evolution in a recirculating loop [6,20]. However, deviation between experiments and ideal FWM dynamics becomes significant very quickly in these cases, and is dramatically impacted by even small amounts of distributed loss or gain [3,14,18]. Consequently, the expected dynamics of isolated FWM have been only partially or imperfectly seen in experiments to date.

Our experimental setup is shown in Fig. 2 and is made of commercially available telecommunications components. First, a laser operating at 1550 nm emits a continuous wave (CW). A phase modulator driven by a 40 GHz RF sinusoidal modulation

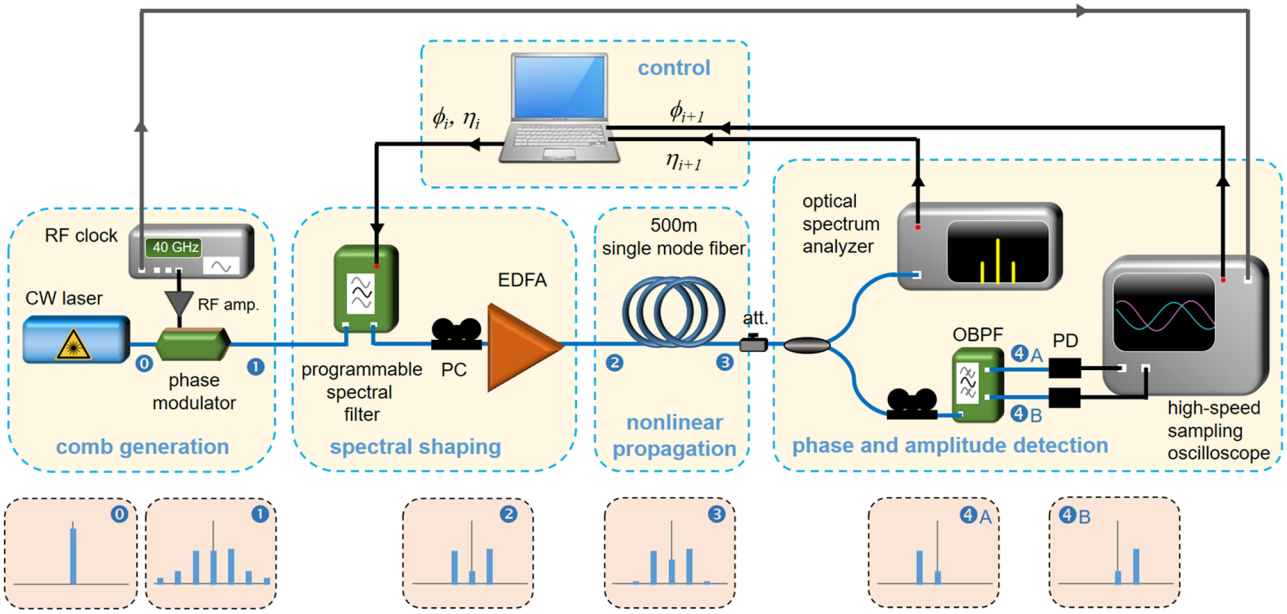

Fig. 2. Experimental setup. Insets 0–4 represent the optical spectrum generated at different stages of the experiment.

converts the monochromatic laser spectrum into a set of equally spaced spectral lines [21]. The resulting symmetrical comb is then processed using a programmable filter (waveshaper device based on liquid crystal on silicon [22]) that simultaneously implements several operations: elimination of unwanted spectral components, and the precise adjustment of the ratio η between the central and lateral components as well as their relative phase ϕ. Special care has been devoted to ensure that no unwanted phase/intensity coupling occurs during this shaping. Specifically, although the finite resolution of a diffraction-based waveshaper necessarily introduces phase–amplitude coupling, this can be mitigated with a sufficient frequency interval between spectral components. In our setup, we found that spacing of 40 GHz or greater avoided such coupling. The tailored three-component signal with targets η_i and ϕ_i is then amplified by an erbium-doped fiber amplifier that can deliver tunable power. The amplifier runs in a power controlled mode so that the average power does not depend on the input spectral properties such that the system can be considered as quasi-conservative.

Nonlinear propagation takes place in single mode optical fiber with dispersion and nonlinear parameters being, respectively, $-7.6\,\mathrm{ps}^2\cdot\mathrm{m}^{-1}$ and $1.7\,\mathrm{W}^{-1}\cdot\mathrm{m}^{-1}$. The fiber length is 500 m, with this length selected as a trade-off between the sensitivity of the detection stage of our setup and the appearance of Brillouin scattering: with 500 m of this fiber, the changes experienced by the optical field are significant enough to be conveniently detected, and we have checked the absence of Brillouin backscattering for the range of powers under investigation. We can therefore work with CW signals without having to involve additional strategies of temporal pulse carving and associated synchronization. To limit polarization mode dispersion, the input state of polarization is optimized using polarization controllers.

The output signal is then attenuated and split in two to record both its spectral phase and intensity. An optical spectrum analyzer (OSA, resolution 0.1 nm) provides directly the ratio η_{i+1}. The spectral phase offset ϕ_{i+1} is retrieved from the temporal delay between the central and lateral sidebands as measured with a high-speed sampling oscilloscope. The experimentally measured values can then be imprinted as new input values, and the process can be iterated at will without any accumulation of deleterious amplified spontaneous emission and without any growth of unwanted spectral sidebands or noise. Potentially unlimited propagation can therefore be emulated.

4. EXPERIMENTAL RESULTS

A. Phase Space and Longitudinal Reconstruction of the Dynamics

We first study the dynamics of the system at maximum gain with $\Omega = \Omega_0 = \sqrt{2}$, i.e., for $P_{in} = 21.5$ dBm. In terms of normalized units, $L_{NL} = 4.1$ km, and the 500 m length of our fiber segment corresponds to a normalized length $\xi_L = 0.12$, similar to the one used in the discussion in Section 2. The experimental phase space portraits obtained for different initial values η_0 and ϕ_0 are shown in Fig. 3(a) with the orbits shown as circles connected by dotted lines. Note that in these experiments, we checked that the energy contained in the unwanted sidebands located at $\pm 2f_m$ always remained well below 3% of the total energy of the signal.

For each value of η_0, we examined the dynamics at two values of initial phase: $\phi_0 = 0$ and $\phi_0 = \pi$ which yielded trajectories on the right and left of the separatrix as expected from the results in Section 2. The dynamics were measured over 25 km (i.e., 50 iterations), and the results yield immediate insight into the phase space topology. The experimental orbits are seen to be in very good agreement with the predictions from the ideal system described in Section 2, which are shown as thick solid lines. Indeed, many fundamental features of the ideal FWM dynamics can be seen from these results. Specifically, we clearly confirm the importance of the separatrix dividing the phase plane into two well-defined regions, with the measurements for $\eta_0 = 0.95$ in particular providing a very clear indication of its location. We also see that the different experimental trajectories are nearly closed orbits and do not intersect. The slight discrepancies between experiment and prediction here are attributed to the accumulation of small errors

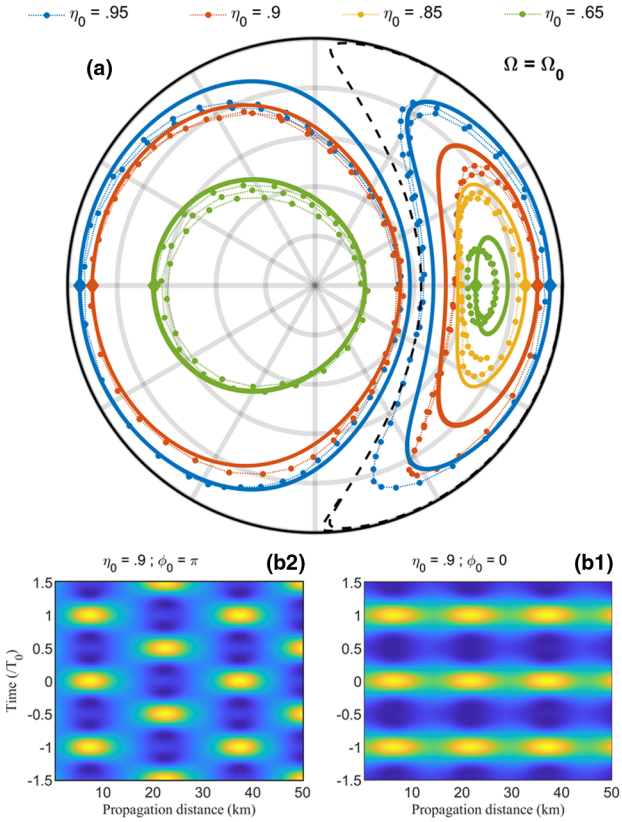

Fig. 3. Experimental results for $\Omega = \Omega_0 = \sqrt{2}$. (a) Phase space portraits for initial values of η_0 of 0.65, 0.85, 0.90, and 0.95 (green, yellow, red, and blue lines, respectively). Results are plotted for an initial phase offset ϕ_0 of 0 or π, which appear, respectively, on the right and left sides of the separatrix (dashed black line). The experimental results over 50 iterations (circles joined with dotted lines) are compared with the theoretical solution of the system (solid thick lines). (b) Longitudinal evolution of the temporal intensity profiles reconstructed from the experimental spectral measurements for η_0 of 0.9 and phases of 0 and π as indicated.

in the phase/intensity measurements and residual depolarization effects not included in our scalar model.

Significantly, with complete experimental knowledge of the spectral phase and intensity of the three interacting frequency components of the evolving field, it is straightforward to fully reconstruct the evolving intensity profiles in the temporal domain. Over a propagation distance of 50 km (normalized distance $\xi = 12$, 100 iterations), Fig. 3(b) shows these results for an initial value of $\eta_0 = 0.9$ and both initial values of phase $\phi_0 = 0$ and $\phi_0 = \pi$ plotted beneath the corresponding orbits on the right and left sides of the phase space plot. These results show the expected recurrence dynamics as seen in Section 2, and for the case of $\phi_0 = \pi$, also highlight the evolution phase shift of half-temporal period, leading, as expected by theory, to a period doubling [15]. Note that these double-periodic solutions have been the subject of particular recent interest [7,18].

B. Influence of Gain

Tuning the input power, we can also explore the modulationally unstable dynamics for higher values of gain. Phase space portraits obtained for an average value of 23.7 dBm, leading to $\Omega = 1.1$ are plotted in Fig. 4. Once again, the experimental results are in good agreement with the theoretical predictions. When comparing with

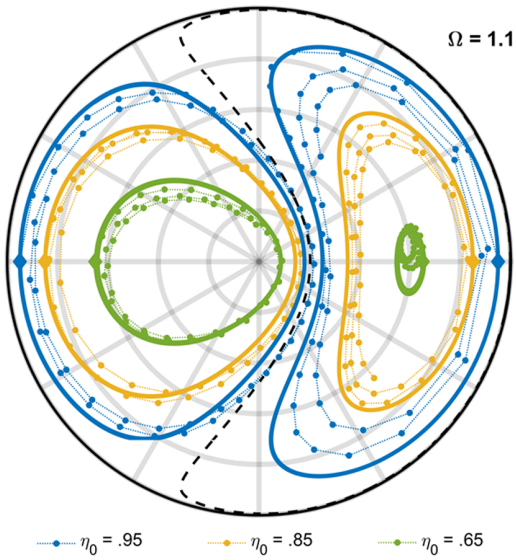

Fig. 4. Experimental phase portraits obtained at an average power $P_{in} = 23.7$ dBm and for initial values of η_0 of 0.65, 0.85, and 0.95 (green, yellow, and blue lines, respectively). Results are plotted for an initial phase offset ϕ_0 of 0 or π, which appear, respectively, on the right and left sides of the separatrix (dashed black line). The experimental results accumulated over 50 iterations (circles joined with dotted lines) are compared with the theoretical solution of the system (solid thick lines).

Fig. 3(a), we note how the dynamics at higher gain are associated with the change in shape of the trajectories and the displacement of the separatrix.

A more exhaustive study of the influence of the average power for a fixed value of $\eta_0 = 0.65$ and $\eta_0 = 0.9$ and phase offset ϕ_0 of 0 and π is shown in Fig. 5. Average powers between 19.7 and 23.7 dBm were tested, leading in terms of normalized frequency Ω to a range between 1.74 and 1.1.

The measurements of the instability process achieved at $\eta_0 = 0.9$ [Fig. 5(a)] confirm that with increasing powers, the separatrix progressively shifts: the intersection point between the separatrix and the horizontal axis $\phi = 0$ continuously decreases. Consequently, the phase space available for the evolution of initial condition $\phi_0 = 0$ gets larger and larger, whereas initial condition $\phi_0 = \pi$ evolves in more and more restricted areas. This shift of the separatrix with power helps to qualitatively understand the reported influence of the losses or gain on FPU recurrence [3,18,23]. Indeed, in the case of losses, the FPU recurrence experienced with $\phi_0 = 0$ is broken as the trajectory crosses the separatrix shifting to the right side. Consequently, phase shifts of half-temporal period appear. In the presence of gain, as the separatrix is moving to the other direction, the in-phase recurrence cycles are preserved.

Further measurements at $\eta_0 = 0.65$ [Fig. 5(b)] are also of interest, especially for $\phi_0 = 0$. Indeed, we note that for the lowest powers (19.7 and 20.2 dBm), the initial condition $\eta_0 = 0.65$ and $\phi_0 = 0$ leads to orbits that are on the left side of the separatrix. For these powers, the trajectory obtained for $\phi_0 = \pi$ is therefore surrounded within the trajectory for $\phi_0 = 0$. When increasing the power, the separatrix is crossed and each initial condition evolves on a different side of the phase plane. For powers between 20.7 and 22.7 dBm, the orbits get smaller and smaller up to the stage where they reach a fixed point for 22.7 dBm. When further increasing the average power, the orbit becomes increasingly open.

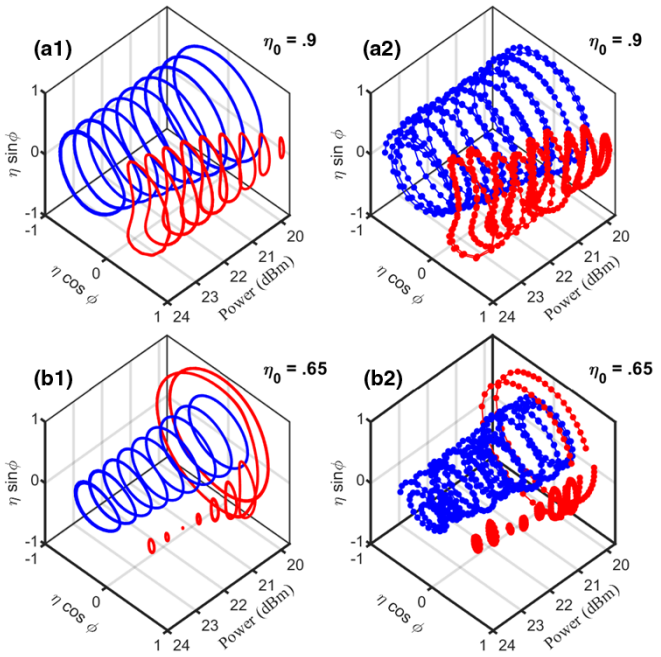

Fig. 5. Influence of the input average power on phase space portraits obtained for initial values of η_0 of (a) 0.9 and (b) 0.65, and initial phase offset of 0 or π. (1) Theoretical predictions are compared with (2) experimental results.

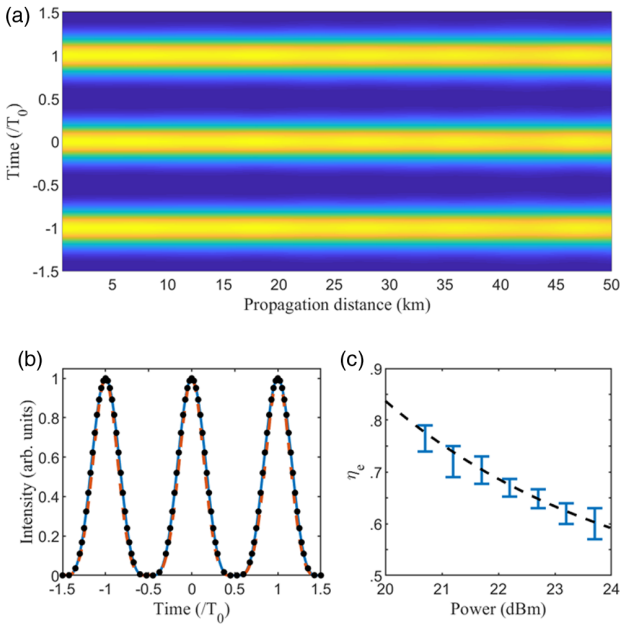

Fig. 6. (a) Longitudinal evolution of the temporal intensity profile reconstructed from the spectral properties of the signal obtained for an average power of 22.7 dBm and initial conditions $\eta_0 = 0.65$ and $\phi_0 = 0$. (b) Comparison of the temporal intensity profile reconstructed from spectral measurements (blue line) and directly measured with an optical sampling oscilloscope (red dashed line). Results from theoretical predictions are also displayed with black circles. (c) Evolution of the value of η_0 leading to a fixed point. The experimental data (blue) are compared with the analytical prediction [dashed black line, Eq. (8)].

C. Observation of a Fixed Point

Finally, we investigate in more detail the properties observed at one of the two fixed points of the phase plane. For $\eta_0 = 0.65$, $\phi_0 = 0$, and $P_{in} = 22.7$ dBm ($\Omega = 1.23$), the longitudinal evolution of the temporal intensity reconstructed from the spectral measurements is plotted in Fig. 6(a) over 50 km. We clearly see in this case that the temporal profile is invariant with propagation. Fig. 6(b) explicitly compares these results with temporal measurements made with a picosecond-resolution optical sampling oscilloscope, and the agreement is such that they cannot be visually distinguished. Moreover, both experimental profiles agree with the expected temporal profile computed from Eq. (3), which in the case of a fixed point, simply consists of a stationary temporal profile formed from three wave interference.

More generally, a fixed point of the ideal FWM system is predicted to exist at any value of gain for a particular choice of sideband ratio. Expressed in terms of normalized frequency Ω, the dependence is given by [13]

$$\eta_e = \frac{3 + \Omega^2}{7}, \tag{8}$$

and this can be readily tested experimentally. Specifically, for different input powers, the waveshaper is used to experimentally determine the value of η_e associated with the fixed point, and the results are shown in Fig. 6(c). The agreement between experimental results (blue) and the prediction of Eq. (8) is excellent.

5. CONCLUSION AND OUTLOOK

Optical systems are well known to provide flexible testbeds with which to study the physics of diverse nonlinear systems, and the results here show the success of a new experimental approach allowing the dynamics of ideal FWM to be fully explored. The use of iterated initial conditions in a short fiber segment mitigates effects of loss, inelastic scattering, and high-order sideband generation, allowing clear observation of the predicted evolution dynamics of the FWM system. Among the dynamics seen are FPU recurrence, qualitatively different evolution on either side of a separatrix, and the existence of system fixed points.

The technique reported here bridges the gap between ideal FWM theory described by coupled differential equations and experiment, allowing us to fully examine the fundamental properties of four wave dynamics using readily available telecommunications components. Indeed, our method using a programmable waveshaper coupled with iterative propagation represents an important technique complementary to earlier approaches studying FWM using recirculation loops [20].

It is important to stress the adaptability of this experimental technique. Potential future investigations are manifold. Although we have focused on spectrally symmetric initial conditions, experiments can easily handle asymmetric initial sidebands [10]. Moreover, our approach can also be readily adapted to study the non-degenerate case that can also be formulated using a Hamiltonian approach, leading to even richer phase space portraits [24]. The two-pump configuration can be extremely fruitful in terms of signal processing capabilities such as optical regeneration or switching [25,26]. Using periodic filtering of unwanted new frequency components could therefore be an effective way to practically improve device performance. Evolution in fibers with normal dispersion [24,27], fourth-order dispersion [28], or dispersion oscillating profiles [29] can also be encompassed as well nonlinear frequency mixing in lumped photonic waveguides [30].

As the state of polarization can also be controlled [31], vector instability processes in birefringent fibers offer additional perspectives [32]. The technique can be extended into the spatial domain and frequency mixing in multimode fiber or waveguides [33,34] using spatial light modulators and phase-intensity characterization [5].

We also anticipate extension to other branches of nonlinear physics where discrete wave mixing plays a central role in system evolution, including route to chaotic evolution [35]. Our method can therefore be translated to hydrodynamics where the use of an initial condition based on the profile of a wave after propagation has already been implemented to reach potentially unlimited propagation distance [36]. This opens the way to a new approach for control of wave dynamics in terms of a reduced set of parameters that affect the phase space trajectory [37].

Funding. Centre National de la Recherche Scientifique (MITI interdisciplinary programs); Conseil régional de Bourgogne-Franche-Comté; Agence Nationale de la Recherche (ANR-15-IDEX-0003, ANR-17-EURE-0002, ANR-20-CE30-0004); Institut Universitaire de France.

Acknowledgment. The numerical simulations used the HPC resources of DNUM CCUB (Centre de Calcul de l'Université de Bourgogne). The authors also thank GDR Elios (GDR 2080).

Disclosures. The authors declare no conflicts of interest.

Data availability. The data that support the findings of this study are available from the corresponding author upon reasonable request.

REFERENCES

1. C. Sulem and P.-L. Sulem, *The Nonlinear Schrödinger Equation: Self-focusing and Wave Collapse* (Springer, 2007), Vol. **139**.
2. A. Mussot, C. Naveau, M. Conforti, A. Kudlinski, F. Copie, P. Szriftgiser, and S. Trillo, "Fibre multi-wave mixing combs reveal the broken symmetry of Fermi–Pasta–Ulam recurrence," Nat. Photonics **12**, 303–308 (2018).
3. O. Kimmoun, H. C. Hsu, H. Branger, M. S. Li, Y. Y. Chen, C. Kharif, M. Onorato, E. J. R. Kelleher, B. Kibler, N. Akhmediev, and A. Chabchoub, "Modulation instability and phase-shifted Fermi-Pasta-Ulam recurrence," Sci. Rep. **6**, 28516 (2016).
4. K. Hammani, B. Wetzel, B. Kibler, J. Fatome, C. Finot, G. Millot, N. Akhmediev, and J. M. Dudley, "Spectral dynamics of modulation instability described using Akhmediev breather theory," Opt. Lett. **36**, 2140–2142 (2011).
5. D. Pierangeli, M. Flammini, L. Zhang, G. Marcucci, A. J. Agranat, P. G. Grinevich, P. M. Santini, C. Conti, and E. DelRe, "Observation of Fermi-Pasta-Ulam-Tsingou recurrence and its exact dynamics," Phys. Rev. X **8**, 041017 (2018).
6. A. E. Kraych, P. Suret, G. A. El, and S. Randoux, "Nonlinear evolution of the locally induced modulational instability in fiber optics," Phys. Rev. Lett. **122**, 054101 (2019).
7. G. Vanderhaegen, C. Naveau, P. Szriftgiser, A. Kudlinski, M. Conforti, A. Mussot, M. Onorato, S. Trillo, A. Chabchoub, and N. Akhmediev, "Extraordinary modulation instability in optics and hydrodynamics," Proc. Natl. Acad. Sci. USA **118**, e2019348118 (2021).
8. R. W. Boyd, *Nonlinear Optics* (Academic, 2003).
9. G. P. Agrawal, *Nonlinear Fiber Optics*, 4th ed. (Academic, 2006).
10. M. E. Marhic, *Fiber Optical Parametric Amplifiers, Oscillators and Related Devices* (Cambridge University, 2008).
11. Y. Chen, "Four-wave mixing in optical fibers: exact solution," J. Opt. Soc. Am. B **6**, 1986–1993 (1989).
12. M. E. Marhic, "Analytic solutions for the phases of waves coupled by degenerate or nondegenerate four-wave mixing," J. Opt. Soc. Am. B **30**, 62–70 (2013).
13. G. Cappellini and S. Trillo, "Third-order three-wave mixing in single-mode fibers: exact solutions and spatial instability effects," J. Opt. Soc. Am. B **8**, 824–838 (1991).
14. G. Van Simaeys, P. Emplit, and M. Haelterman, "Experimental study of the reversible behavior of modulational instability in optical fibers," J. Opt. Soc. Am. B **19**, 477–486 (2002).
15. S. Trillo and S. Wabnitz, "Dynamics of the nonlinear modulational instability in optical fibers," Opt. Lett. **16**, 986–988 (1991).
16. J. R. Thompson and R. Roy, "Nonlinear dynamics of multiple four-wave mixing processes in a single-mode fiber," Phys. Rev. A **43**, 4987–4996 (1991).
17. S. Pitois, J. Fatome, and G. Millot, "Generation of 160-GHz transform-limited pedestal-free pulse train trough multiwave mixing compression of a dual frequency beat signal," Opt. Lett. **27**, 1729–1731 (2002).
18. C. Naveau, G. Vanderhaegen, P. Szriftgiser, G. Martinelli, M. Droques, A. Kudlinski, M. Conforti, S. Trillo, N. Akhmediev, and A. Mussot, "Heterodyne optical time domain reflectometer combined with active loss compensation: a practical tool for investigating Fermi Pasta Ulam recurrence process and breathers dynamics in optical fibers," Front. Phys. **9**, 637812 (2021).
19. X. Hu, W. Chen, Y. Lu, Z. Yu, M. Chen, and Z. Meng, "Distributed measurement of Fermi–Pasta–Ulam recurrence in optical fibers," IEEE Photon. Technol. Lett. **30**, 47–50 (2018).
20. J.-W. Goossens, H. Hafermann, and Y. Jaouën, "Experimental realization of Fermi-Pasta-Ulam-Tsingou recurrence in a long-haul optical fiber transmission system," Sci. Rep. **9**, 18467 (2019).
21. K. Hammani, J. Fatome, and C. Finot, "Applications of sinusoidal phase modulation in temporal optics to highlight some properties of the Fourier transform," Eur. J. Phys. **40**, 055301 (2019).
22. A. M. Clarke, D. G. Williams, M. A. F. Roelens, and B. J. Eggleton, "Reconfigurable optical pulse generator employing a Fourier-domain programmable optical processor," J. Lightwave Technol. **28**, 97–103 (2010).
23. F. Coppini, P. G. Grinevich, and P. M. Santini, "Effect of a small loss or gain in the periodic nonlinear Schrödinger anomalous wave dynamics," Phys. Rev. E **101**, 032204 (2020).
24. S. Trillo, S. Wabnitz, and T. Kennedy, "Nonlinear dynamics of dual-frequency-pumped multiwave mixing in optical fibers," Phys. Rev. A **50**, 1732–1747 (1994).
25. M. E. Marhic, P. A. Andrekson, P. Petropoulos, S. Radic, C. Peucheret, and M. Jazayerifar, "Fiber optical parametric amplifiers in optical communication systems," Laser Photon. Rev. **9**, 50–74 (2015).
26. Z. Tong and S. Radic, "Low-noise optical amplification and signal processing in parametric devices," Adv. Opt. Photon. **5**, 318–384 (2013).
27. A. Barthelemy and R. De La Fuente, "Unusual modulation instability in fibers with normal and anomalous dispersions," Opt. Commun. **73**, 409–412 (1989).
28. X. Yao, C. Liu, Z.-Y. Yang, and W.-L. Yang, "Heteroclinic-structure transition of the pure quartic modulation instability," Phys. Rev. Res. **4**, 013246 (2022).
29. M. Conforti, A. Mussot, A. Kudlinski, S. R. Nodari, G. Dujardin, S. De Biévre, A. Armaroli, and S. Trillo, "Heteroclinic structure of parametric resonance in the nonlinear Schrödinger equation," Phys. Rev. Lett. **117**, 013901 (2016).
30. H. Fukuda, K. Yamada, T. Shoji, M. Takahashi, T. Tsuchizawa, T. Watanabe, J. Takahashi, and S. Itabashi, "Four-wave mixing in silicon wire waveguides," Opt. Express **13**, 4629–4637 (2005).
31. O. Masihzadeh, P. Schlup, and R. A. Bartels, "Complete polarization state control of ultrafast laser pulses with a single linear spatial light modulator," Opt. Express **15**, 18025–18032 (2007).
32. S. G. Murdoch, R. Leonhardt, and J. D. Harvey, "Nonlinear dynamics of polarization modulation instability in optical fiber," J. Opt. Soc. Am. B **14**, 3403–3411 (1997).
33. M. Guasoni, F. Parmigiani, P. Horak, F. Fatome, and D. J. Richardson, "Intermodal four-wave mixing and parametric amplification in kilometer-long multimode fibers," J. Lightwave Technol. **35**, 5296–5305 (2017).
34. C. Lacava, M. A. Ettabib, T. D. Bucio, G. Sharp, A. Z. Khokhar, Y. Jung, M. Sorel, F. Gardes, D. J. Richardson, P. Petropoulos, and F. Parmigiani, "Intermodal Bragg-scattering four wave mixing in silicon waveguides," J. Lightwave Technol. **37**, 1680–1685 (2019).
35. J. R. Thompson and R. Roy, "Statistical fluctuations in multiple four-wave mixing in a single-mode optical fiber," Phys. Rev. A **44**, 7605–7614 (1991).
36. A. Chabchoub, N. Hoffmann, M. Onorato, and N. Akhmediev, "Super rogue waves: observation of a higher-order breather in water waves," Phys. Rev. X **2**, 011015 (2012).
37. A. Gomel, A. Chabchoub, M. Brunetti, S. Trillo, J. Kasparian, and A. Armaroli, "Stabilization of unsteady nonlinear waves by phase-space manipulation," Phys. Rev. Lett. **126**, 174501 (2021).